

# Experimental studies of equilibrium vortex properties in a Bose-condensed gas

I. Coddington, P. C. Haljan, P. Engels, V. Schweikhard, S. Tung and E. A. Cornell\*

*JILA, National Institute of Standards and Technology and Department of Physics,  
University of Colorado, Boulder, Colorado 80309-0440*

(Dated: November 1, 2018)

We characterize several equilibrium vortex effects in a rotating Bose-Einstein condensate. Specifically we attempt precision measurements of vortex lattice spacing and the vortex core size over a range of condensate densities and rotation rates. These measurements are supplemented by numerical simulations, and both experimental and numerical data are compared to theory. Finally, we study the effect of the centrifugal weakening of the trapping spring constants on the critical temperature for quantum degeneracy and the effects of finite temperature on vortex contrast.

PACS numbers: 03.75.Lm, 67.90.+z, 67.40.Vs, 32.80.Pj

## I. INTRODUCTION

After the initial observations of vortex lattices in Bose-Einstein condensed gases [1, 2, 3, 4], most of the experimental work has focused on dynamical behavior of vortices and lattices, including Kelvons [5, 6, 7], Tkachenko waves [8, 9, 10, 11, 12, 13], and various nonequilibrium effects [14, 15]. Equilibrium properties, in contrast, have been relatively neglected by experimenters. This imbalance is not indicative of a lack of interesting physics in equilibrium behavior, but simply reflects the usual experimentalist's preference for measuring spectra rather than static structure. Theorists, on the other hand, have investigated equilibrium properties extensively [16, 17, 18, 19, 20, 21, 22, 23, 25, 26, 27, 28], and our purpose in this paper is to partially redress this imbalance with a series of experimental studies focusing on equilibrium properties of rotating condensates.

The vortex lattice in a rotating Bose-condensed gas naturally organizes into a regular triangular lattice, or Abrikosov lattice, originally observed in superconductors. The lattice can be well characterized by the nearest-neighbor lattice spacing and by the radius of each vortex core ( $b$  and  $r_v$  respectively for the purpose of this paper). The nearest-neighbor lattice spacing,  $b$ , is generally thought to be determined only by the rotation rate when in the high-rotation regime where the rotating BEC exhibits nearly rigid-body behavior. Numerical work [16] and early analytical work [8], however, suggests that this rigid-body assumption yields lattice constants that are smaller than would be seen in the case of a finite-size trapped BEC. Recent work by Sheehy and Radzihovsky [17] has tackled analytically this discrepancy and found it to be a necessary consequence of the inhomogeneous density profile of the condensate. With this theory they address the question of why the lattice is so remarkably regular given the condensate density profile. They also derive a small, position-dependent, inhomogeneity-induced correction term to the lattice spacing. An interesting implication of this theory is that the vortices must move slightly faster than the surrounding superfluid

even near the rigid-body limit. More striking still is the prediction that the superfluid should exhibit a radially-dependant angular velocity (or radial shear flow), which directly follows from their calculation of inhomogeneous vortex density. While a differential rotation rate is not directly observable in our system, the position-dependent variation of the nearest-neighbor lattice spacing is studied in Sec. II below. It should also be noted that the inhomogeneity in the areal density of vortices, predicted in Ref. [17], can also be derived in the limit of the lowest Landau level (LLL). This property of the LLL was first brought to our attention by A.H. MacDonald and has been the subject of two recent publications by Watanabe *et al.* [18] and Cooper *et al.* [19].

The second effect we study in this paper concerns the core size of the vortices. Once rotation rate and density are fixed, the vortex core size is a length scale that the condensate chooses on its own. In this sense vortex core size constitutes a fundamental property of the system and has therefore been the subject of much theoretical work [20, 21, 22]. By analogy to superfluid  $^4\text{He}$ , the core size is dictated by the atomic interactions and is of order of the healing length. For our system the healing length is only one and a half times the average interatomic spacing. Because of this diluteness one might wonder if there are certain regimes of sufficiently low or high density where one would see a deviation from mean-field theory. Investigation of core size makes up Sec. III of this paper.

It has been predicted [23] that at higher rotation the condensate begins to enter the LLL regime where the condensate wave function is constrained to occupy only the LLL harmonic oscillator states. Our condensate is strikingly different from quantum Hall systems also associated with the LLL in that the mean-field approximation is still a valid way to account for interactions. In this case the vortex core-size to lattice-spacing ratio saturates at the LLL limit [24, 29]. As Baym and Pethick [25] note this requires the cores to deviate from the Thomas-Fermi prediction in shape and size.

Employing a numerically generated Gross-Pitaevskii

(GP) wave function, we study this transition and monitor the core size and shape over a range of conditions. These simulations show a smooth transition from the Thomas-Fermi regime to the LLL regime. Additionally we use numerical analysis to study the shape of the vortex cores and verify that when the core-area saturation occurs the vortex-core wave function is the one predicted for the LLL regime. This result suggests that the fractional core area is a possible means to probe the transition to the LLL regime. To test this idea, we compare simulations with experimental data. This comparison and possible systematic errors in these experimental measurements are discussed in Sec. III B.

In Sec. IV we examine the rotational suppression of quantum degeneracy. This effect is due to centrifugal forces weakening the radial trap-spring constants. Weaker spring constants then lead, in a straight forward way, to a lower critical temperature for fixed numbers of atoms.

Finally in Sec. V we examine a proposal that a measurement of the contrast of vortex cores could serve as a sensitive thermometer for a condensate in the regime for which the temperature is less than the chemical potential and other methods of thermometry become unreliable. In Sec. V we discuss our preliminary efforts to realize this vision. We are able to see an effect, but we have not yet been able to extend this measurement technique below the usual limits.

The rest of Sec. I discusses experimental issues common to all the results of this paper

### A. Experiment

Our experiment begins with a magnetically trapped cloud containing greater than  $10^7$   $^{87}\text{Rb}$  atoms in the  $|F = 1, m_F = -1\rangle$  hyperfine ground state, cooled to a temperature roughly three times the critical temperature ( $T_c$ ) for Bose condensation. Using a TOP trap we confine these atoms in an axially symmetric, oblate and harmonic potential with trapping frequencies ( $\{\omega_\rho, \omega_z\} = 2\pi\{7, 13\}\text{Hz}$ ) with axis of symmetry along the vertical ( $z$ ) axis. Rotation is generated in the thermal cloud by resonantly coupling to a scissors mode of the cloud [30, 31]. To do this we gradually apply an elliptical deformation to the magnetic trapping potential by distorting the amplitude of the rotating TOP field in time. The resulting distorted trap has roughly similar average radial-trapping frequency but an ellipticity [32] in the horizontal plane of 25%. The uncondensed cloud is held in this trap for 5 seconds while any excitations die out. At this point the angle of the major axis of the elliptically distorted trapping field is jumped quickly by 45 degrees in the horizontal plane to generate the initial conditions of the scissors mode. From here the cloud is allowed to evolve for 155 ms, or roughly one quarter period of the result-

ing scissors mode, at which point we transfer the cloud to a radially symmetric trap. Essentially we have caught the scissors oscillation between turning points where all the initial linear velocity has turned into rotational velocity. Using this method we can generate a cloud rotating at roughly half the radial trap frequency, with minimal heating. By lowering the amplitude of the trap distortion or the angle by which the trap is jumped, we can easily generate more slowly rotating clouds as well.

At this point we begin a second phase of rf evaporation, but this time we evaporate in one dimension along the axis of rotation [4]. The motivation for this seemingly inefficient technique is that the 1D evaporation allows us to remove energy from the  $z$  axis of the condensate without preferentially removing high angular momentum atoms. Lowering the energy per particle without lowering the angular momentum per particle accelerates the cloud rotation rate  $\Omega$ . To perform this 1D evaporation, we adiabatically ramp to a prolate geometry ( $\{\omega_\rho, \omega_z\} = 2\pi\{8.3, 5.3\}\text{Hz}$ ) where the rest of the experiment is carried out.

Reaching significant rotation rates by the end of evaporation requires that the lifetime of the thermal cloud's angular momentum be comparable to the evaporation time. The nearly one-dimensional nature of the evaporation together with the low average trap frequencies makes cooling to BEC in the prolate trap very slow (2 minutes). We obtain angular momentum lifetimes this long by shimming the TOP trap's rotating bias field to cancel the few percent azimuthal trap asymmetry that exists despite careful construction. With this technique we suppress the azimuthal trap ellipticity to less than one part in a thousand.

After the evaporation we have a condensate with as many as 4.5 million atoms and rotation rates from  $\Omega = (0 - 0.975)\omega_\rho$ , with no observable thermal cloud. Rotation can be accurately determined by comparing the condensate aspect ratio  $\lambda$  (defined as the axial Thomas-Fermi radius over the radial Thomas-Fermi radius  $R_z/R_\rho$ ) to the trap aspect ratio  $\lambda_0 \equiv (\omega_\rho/\omega_z)$ , and using the now standard relation

$$\Omega/\omega_\rho = \sqrt{(1 - (\lambda/\lambda_0)^2)} . \quad (1)$$

### B. Expansion

The clouds described here typically contain between 1-200 vortices, each of which is too small to be observed in-trap but can be seen after expansion of the cloud. Our expansion technique, while not completely unique, is unusual enough to warrant a description. For the experiments presented here and elsewhere, we need a large radial expansion to make sure that the vortex cores are large compared to our imaging resolution. Additionally we need to suppress the axial expansion in order to pre-

serve certain length scales in the condensate as discussed below. Clearly, given our low and nearly isotropic trap frequencies, the usual expansion technique of shutting off the magnetic field and dropping the cloud would not meet such requirements. The solution, which has been demonstrated by other groups [33], is to perform an anti-trapped expansion. Rather than simply shutting off the trapping potential, we invert the trap in the radial direction so that the cloud is actively pulled apart. Simultaneously, the magnetic field gradient in the vertical direction is used to support against gravity. Because it has generated some interest we describe this technique in the following paragraph in what otherwise might be excessive detail.

The expansion is achieved in several steps that take place in rapid succession. First we employ a microwave adiabatic rapid passage technique (ARP) to transfer the atoms from the weak-field seeking  $|F = 1, m_F = -1\rangle$  state to the strong-field seeking  $|F = 2, m_F = -1\rangle$  state. The microwave field employed is powerful enough to perform the transfer in  $10\mu s$  but, as will be discussed shortly, we often take as long as  $300\mu s$  for this transfer. After transfer to the anti-trapped state, the cloud still sits in its original position below the quadrupole zero, which means that both gravity and the magnetic field are acting to pull it downward. To counter this force a downward uniform vertical magnetic field is added to pull the quadrupole zero below the condensate so that the magnetic field gradient again cancels gravity. The field is applied within  $10\mu s$ , fast compared to relevant time scales. In this manner the cloud is again supported against gravity. To reduce curvature in the  $z$  direction, the TOP trap's rotating bias field is turned off leaving only the linear magnetic gradient of the quadrupole field. This gradient is tuned slightly to cancel gravity.

Using this technique, we are able to radially expand the cloud by more than a factor of 10 while, at the same time, seeing less than a factor of two axial expansion. Unfortunately even this much axial expansion is unacceptable in some cases. In the limit of adiabatic expansion, this factor of two decrease in condensate density would lead to an additional  $\sqrt{2}$  increase in healing length during expansion. Thus, features that scale with healing length, such as vortex core radius in the slow rotation limit, would become distorted. The effect of axial expansion on vortex size was first noted by Dalfvo and Modugno [34].

To suppress the axial expansion, we give the condensate an initial inward or compressional impulse along the axial direction. This is done by slowing down the rate at which we transfer the atoms into the anti-trapped state. The configuration of the ARP is such that it transfers atoms at the top of the cloud first and moves down through the cloud at a linear rate. These upper atoms are then pulled downward with a force of  $2g$  (gravity plus magnetic potential), thus giving them an initial inward impulse. Finally, the ARP sweep passes resonantly

through the lowest atoms in the cloud: they, too, feel a downward acceleration but the axial magnetic field gradient is reversed before they can accumulate much downward velocity. On average the cloud experiences a downward impulse, but also an axial inward impulse. Normally the ARP happens much too fast for the effect to be observable but when the transfer time is slowed to  $200 - 300\mu s$  the effect is enough to cause the cloud to compress axially by 10-40% for the first quarter of the radial expansion duration. The cloud then expands back to its original axial size by the end of the radial expansion.

Despite our best efforts to null out axial expansion, we observe that the cloud experiences somewhere between 20% axial compression to 20% axial expansion at the time of the image, which should be, at most, a 10% systematic error on measured vortex core radius. The overall effect of axial expansion can be seen in Fig. 1, where image (b) and (c) are similar condensates and differ primarily in that (c) has undergone a factor of 3 in axial expansion while in (b) axial expansion has been suppressed. The effect on the vortex core size is clearly visible.

Because almost all the data presented in this paper is extracted from images acquired after the condensate expands, it is worth discussing the effect of radial expansion on the density structure in the cloud. In the Thomas-Fermi limit, it is easy to show that the anti-trapped expansion in a parabolic trap, combined with the mean-field and centrifugally driven expansion of the rotating cloud, leads to a simple scaling of the linear size [35] of the smoothed, inverted-parabolic density envelope. As  $R_\rho$  increases, what happens to the vortex-core size? There are two limits that are easy to understand. In a purely 2D expansion (in which the axial size remains constant), the density at any spot in the condensate co-moving with the expansion goes as  $1/R_\rho^2$ , and the local healing length  $\xi$  then increases over time linearly with the increase in  $R_\rho$ . In equilibrium, the vortex core size scales linearly with  $\xi$ . The time scale for the vortex core size to adjust is given by  $\hbar/\mu$  where  $\mu$  is the chemical potential. In the limit (which holds early in the expansion process) where the fractional change in  $R_\rho$  is small in a time  $\hbar/\mu$ , the vortex core can adiabatically adjust to the increase in  $\xi$ , and the ratio of the core-size to  $R_\rho$  should remain fixed as the cloud expands.

In the opposite limit, which applies when  $R_\rho$  expands very rapidly compared to  $\hbar/\mu$ , the inverted parabolic potential dominates the dynamics, and every point in the cloud expands radially outward at a rate proportional to its distance from the cloud center. In this limit, the “fabric of the universe” is simply stretched outward, and all density features, including vortex core size expand at the same fractional rate. Again, the ratio of core-size to  $R_\rho$  should remain fixed.

So in the two extreme limits, the ration of vortex core size to  $R_\rho$  (and other density features, such as nearest-

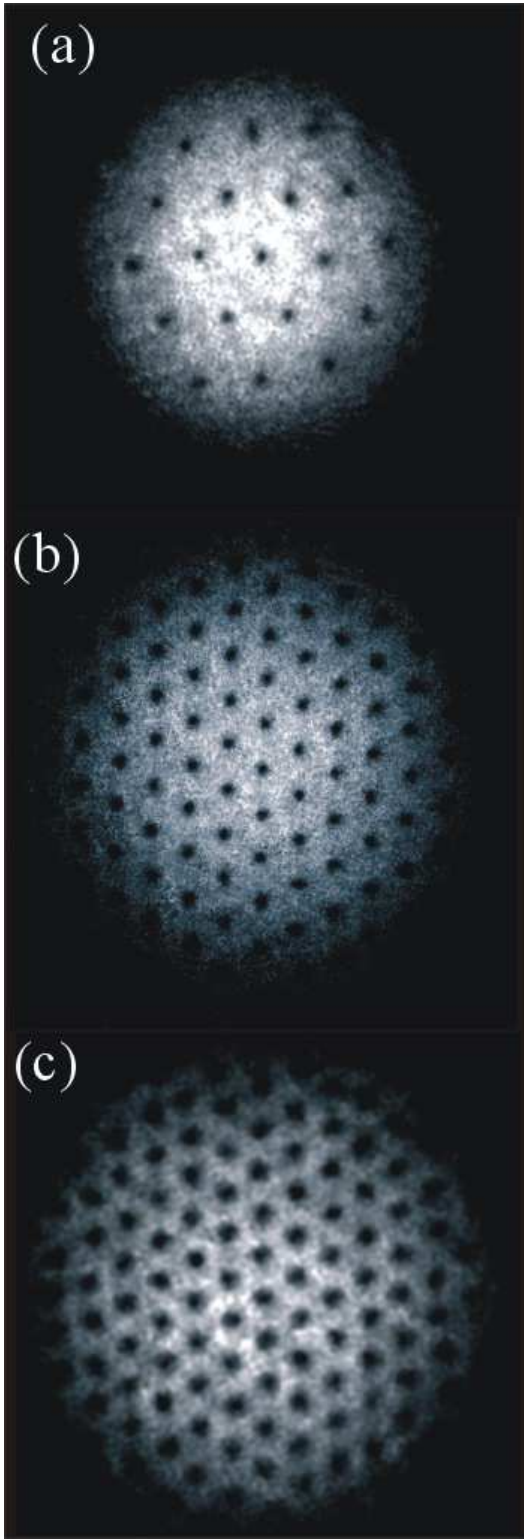


FIG. 1: Examples of the condensates used in the experiment viewed after expansion. Image (a) is a slowly rotating condensate. Images (b) and (c) are of rapidly-rotating condensates with similar in-trap conditions. They differ only in that (c) was allowed to expand axially during the anti-trapped expansion. The effect on the vortex core size is visible by eye. Images (a) and (b) are of the regularity required for the nearest-neighbor lattice spacing measurements.

neighbor vortex separation) remains fixed. It is reasonable then to assume that this behavior will be true in general in the intermediate regime between the two expansion rates. Extensive numerical simulations were performed to validate this assumption.

On a separate note, the vortex lattice spacing, unlike vortex core size, is largely unaffected by the presence of axial expansion. However, we see some indication that deep in the lowest Landau level large axial expansions can affect vortex spacing as well as size.

Once expanded, the cloud is imaged along the vertical direction, and data is extracted by fitting the integrated (along the line of sight) condensate density profile with a Thomas-Fermi distribution. We then subtract this fit from the image and easily fit the remaining vortex-core residuals with individual 2D Gaussian profiles to determine the core centers and radii. For the purpose of this paper the vortex radius  $r_v$  is defined to be the RMS radius of the 2D Gaussian that we fit to the core. For clarification, the RMS radius of a 2D Gaussian would be 0.60 times its FWHM. Condensate and vortex fits can be performed iteratively to reduce error.

Before each expanded image we also take a horizontal, nondestructive, in-trap image of the cloud immediately before expansion. From this image, rotation rate and atom number are determined. Length scales in the expanded cloud can be scaled back to in-trap values by dividing by the radial expansion factor, defined as  $R_\rho(\text{expanded})/R_\rho(\text{in-trap})$ .

### C. Numerical studies

The numerical studies discussed in this paper are done by setting up an initial in-trap condensate wave function with a given  $N$  and  $\Omega$  on a  $2048 \times 2048$  lattice and then relaxing this wave function by propagating the Gross-Pitaevskii equation in imaginary time. All work shown in Sec. III B and III C is done in 2D. Additionally a radially symmetric 3D simulation can be performed for a single vortex, as is done in Sec. III A. Once the final wave function is found, we convert to an atom density profile which can be fit and analyzed in the same manner as the experimental data.

## II. THE LATTICE CONSTANT

At first sight, vortex lattices, such as the one seen in Fig. 1(b), appear perfectly regular. However as noted in the introduction, Sheehy and Radzihovsky [17] predict that there should exist a small correction to the vortex density in the condensate due to the condensate, density inhomogeneity. One result from Ref. [17] is that the

areal density of vortices is

$$n_v(\rho) = \frac{\Omega m}{\pi \hbar} - \frac{1}{2\pi R_\rho^2 (1 - (\rho/R_\rho)^2)^2} \ln[\hbar/(2.718 m \Omega \xi^2)], \quad (2)$$

where  $m$  is the mass of rubidium and  $\xi$  is the healing length (calculated from the measured density). This equation can conveniently be thought of as the rigid body rotation (first term) plus the density inhomogeneity correction that reduces vortex density. We compare to experimental measurements by converting vortex density to a nearest-neighbor lattice spacing, conveniently expressed in units of condensate radius

$$b(\rho) = \sqrt{2/(3^{1/2} n_v(\rho))} \frac{1}{R_\rho}. \quad (3)$$

To study this lattice inhomogeneity effect experimentally, we generate condensates with rotation rates of  $\Omega/\omega_\rho = 0.5 - 0.9$ . To extract the vortex separation, we expand the cloud by a factor of 10 in the radial direction using the anti-trapped expansion technique. The condensate and vortices are fit as described in Sec. I B. The nearest-neighbor separation for a given vortex is measured by averaging the distance from the vortex center to the centers of the six nearest vortices. Because of low signal, vortices further than  $0.9 R_\rho$  from the condensate center are disregarded. Any remaining vortex with fewer than six nearest neighbors (i.e., a vortex in the outer ring) is used as a neighbor to other vortices but is not itself included in the final data. Obviously using the six nearest neighbors assumes a triangular lattice structure, so before fitting, each image is checked for defects in the lattice. Any image exhibiting broken lattice planes is not considered. Once the nearest-neighbor separation is measured, it is normalized by the expanded condensate radius to compare to Eq. 3. For this comparison,  $R_\rho$ ,  $\Omega$ , and  $\xi$  are measured or calculated from an in-trap image. To improve the theory fit, we allowed  $R_\rho$  to be an adjustable theory parameter, but, in each case, the theory fit value for  $R_\rho$  was within 5% of the experimentally determined value of  $R_\rho$ . This  $< 5\%$  difference is within the calibration uncertainty for such a measurement. Noise is suppressed by taking an azimuthal average of the lattice spacing data. Due to the discrete nature of the vortices this is equivalent to binning the lattice-spacing data by radial displacement of the vortex from the condensate center.

Figure 2 shows a comparison to theory for three physical condensates and one numerically generated condensate density profile. Figure 2(a) is data taken from the condensate in Fig. 1(a). The two points shown correspond to the measured vortex density for the center vortex (first point) and the average vortex density for the first ring of vortices. Also plotted is Eq. 3 (solid line) and the expected nearest-neighbor lattice spacing for rigid body rotation (dashed line). The imperfect fit may be

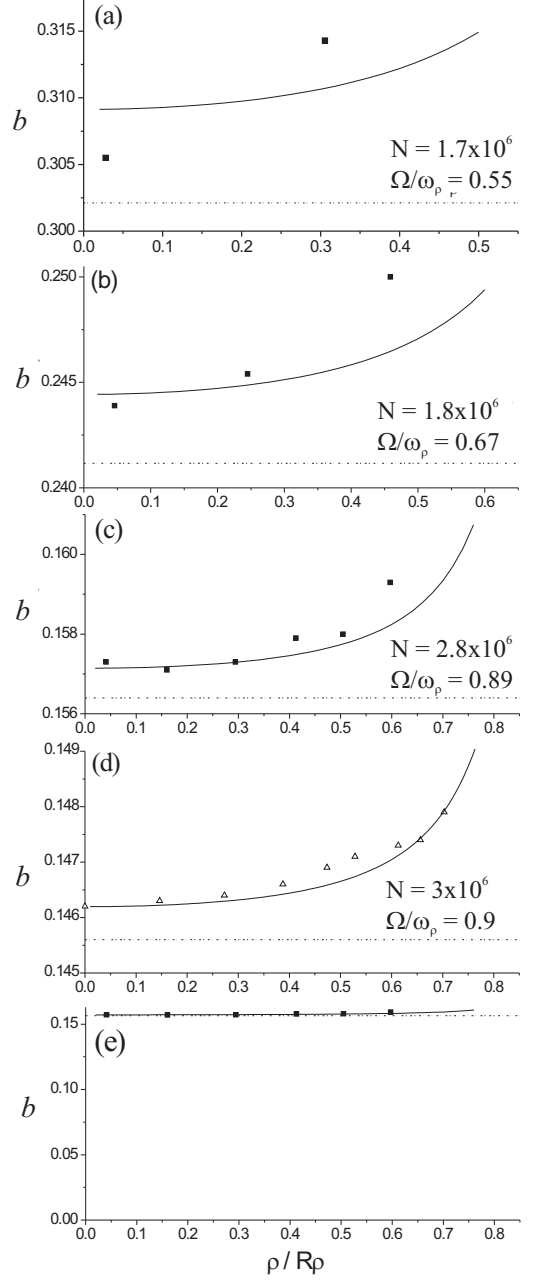


FIG. 2: Measured and binned lattice spacings as a function of radial position  $\rho$ . The solid curve is the theory result (Eq. (3)) of Sheehy and Radzihovsky [17]. The rigid-body-rotation rate lattice spacing is also plotted for comparison (dashed line). Plots (a-c) are experimental data with increasing rotation. Plot (a) and (c) are data taken from the condensate in Figs. 1(a) and (b), respectively. Plot (d) is the same effect observed in the numerical data. One can see that theory and experiment show a similar dependence on radial position and that the fractional amplitude of the density inhomogeneity effect is suppressed at higher rotation. Plot (e) is the data in (c) plotted without suppressing the zero. The vortex lattice spacing changes less than 2% over a region in which the atom density varies by 35%.

partly due to the discrete nature of the data, vis-a-vis a continuum theory [17]. Plots (b) and (c) are condensates with increasing rotation rates where (c) is taken from image 1(b). Plot (d) is a comparison with numerical data prepared with parameters similar to the experimental situation in (c). Figure 2(e) is the same data in Fig. 2(c) but plotted without the suppressed zero to emphasize the smallness of the position dependant effect. The areal density of vortices is constant to 2% over a region that experiences an atom-density variation of 35%.

### III. VORTEX CORES

#### A. Core size

The other defining length scale of the vortex lattice is the core radius. Here we study the core radius in the Thomas-Fermi regime (as opposed to the lowest Landau level regime, described later) where it should scale with the healing length. A theoretical value for the vortex core radius was generated by performing a numerical simulation for a 3D BEC containing an isolated vortex and comparing the fitted radius of this vortex to the corresponding healing length. Fitting the simulation in the same manner that we later treat the experimental data (described in Sec. I B) we obtain an expression for the core radius of

$$r_v = 1.94 \times \xi, \quad (4)$$

with healing length  $\xi = (8\pi n a_{sc})^{-1/2}$ , where  $a_{sc}$  is the scattering length and  $n$  is the density-weighted atom density. For the data presented,  $n$  is determined from the in-trap image before expansion.

Core size measurements and fractional core area (discussed in the next subsection) measurements require considerable attention to detail. In pursuing these measurements, we find that nearly everything — from focusing issues, to lensing due to off resonant imaging light, to even imperfect atom transfer into the anti-trapped state before expansion — can lead to an overestimation of the vortex core size. By far the biggest potential systematic error in our system is axial expansion, which, as noted in Sec. I B, requires careful attention.

A range of core sizes is achieved by varying the initial number of atoms loaded into the magnetic trap prior to evaporation. To avoid the core size saturation effect, due to high condensate rotation [25], we consider only clouds with  $\Gamma_{LLL} > 10$ , where  $\Gamma_{LLL} \equiv \mu/(2\hbar\Omega)$  is the LLL parameter and  $\mu$  is the chemical potential. This ratio of chemical potential to rotation approaches unity as we enter the LLL regime, while at values of 10 or greater we should be firmly in the Thomas-Fermi regime. In practice this requires only that we keep the condensate rotation rate low. Core size is measured by fitting the

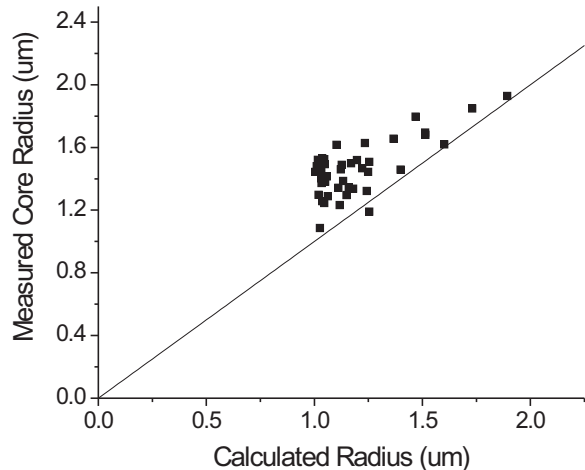


FIG. 3: Comparison of measured core radii with the Thomas-Fermi prediction (Eq. (4)) represented by the solid line. Black squares are the core size in expansion scaled by the radial expansion of the condensate so that they correspond to the in-trap values. Data shows reasonable agreement with theory. The fact that the measured core size is consistently larger is likely due to the fact that nearly all our imaging systematics lead to an overestimation of the vortex core size.

expanded image with a Thomas-Fermi profile and each core with a 2D Gaussian. For Fig. 3 the measured core radius in expansion is scaled back to the corresponding in-trap value using the radial expansion factor discussed in Sec. I B. To reduce scatter we consider only vortices located less than half a condensate radius out from the center. Additionally we find that some vortices appear to have some excitation or bending which leads to a poor fit. To filter these out we consider only vortices that have a contrast greater than 0.6. Here contrast is defined, with respect to the integrated (along the line of sight) condensate profile, as the peak of the “missing” column density at the vortex position divided by the smoothed Thomas-Fermi profile at the same position. On average, about 30% of visible vortices fulfill all the criteria for being used in the core size measurement, although this number can vary wildly (10%-100%) depending on vortex number and position.

From Fig. 3 we can see that the data and the Thomas-Fermi theory agree reasonably well. The data do seem to be slightly above the theory value, but we are hesitant to make too much of this because, as noted before, there are many systematic errors that tend to bias the data toward larger core size. Measurement is easier and the agreement better, on the low density, large-core side of the graph.

At an early stage in this work, we speculated that the mean-field Gross-Pitaevskii equation might not give

a good quantitative description of vortex core size because the core size is particularly sensitive to the healing length  $\xi$ . At our highest densities, while the gas is nominally dilute ( $na_{sc}^3 < 10^{-5}$ , where  $a_{sc}$  is the interatomic scattering length), the mean interatomic distance  $n^{-1/3}$  is only a factor of 1.5 less than  $\xi$ . Our data, however, are ambiguous with respect to the accuracy of the Gross-Pitaevskii equation for predicting vortex core sizes at our highest densities. The roughly 25% discrepancy between our measurements and the mean-field prediction shown at the smaller radii in Fig. 3 is comparable to possible systematic errors in our measurements of the smaller cores that exist at higher densities. In retrospect, our experimental design is such that we may be unable to see a mean-field failure even if one were to exist. During the radial expansion, the density drops. Thus the accuracy of the mean-field approximation is likely to improve significantly during the expansion. Our anti-trapped expansion, while more rapid than a conventional ballistic expansion, is still slow compared to the rate at which a vortex can adiabatically relax its radius [25] (approximately  $\mu/\hbar$ ). Any non-mean-field corrections to the vortex core size will likely relax away before the cores have expanded to be large enough for us to reliably image them [36].

### B. Fractional core area

As noted in the introduction, the fractional condensate area occupied by the vortex cores is also a quantity that has been of much theoretical interest [16, 25, 27] and has been experimentally studied previously [29]. It is argued by Baym and Pethick [25] that the fractional core area reaches a limiting value as one enters the LLL regime. The corollary of this argument is that fractional core area is a reasonable way to monitor the transition to the lowest Landau level regime. We examine this transition with numerical work, which we can push further into this regime than we can achieve experimentally. Additionally we examine some of the systematic errors that can affect the experimental data. To this end numerical calculations were performed as previously described, for  $3 \times 10^6$ ,  $5 \times 10^5$ , and  $1 \times 10^5$  atoms, and for rotations ranging from  $\Omega/\omega_p = 0.15$  to 0.998. For the experimental data, actual condensates were generated over a similar range with  $\Omega/\omega_p = 0.15$  to 0.98 and  $N = 4 - 50 \times 10^5$ . The numerical data as well as the experimental data are fit in the same manner as described in Sec. I B.

We define the fractional area  $\mathcal{A}$  occupied by the vortices to be  $\mathcal{A} = n_v \pi r_v^2$ , where  $n_v$  is the areal density of vortices and  $r_v^2$  is defined in Eq. 4. Ignoring density inhomogeneity effects, in the limit of many vortices, the expected vortex density  $n_v$  is  $m\Omega/(\pi\hbar)$ . The resulting prediction for  $\mathcal{A}$  can be expressed as  $\mathcal{A} = 1.34 \times \Gamma_{LLL}^{-1}$ . This value exceeds unity for  $\Gamma_{LLL} < 1.34$ , which has led to the prediction that vortices should merge as the con-

densate enters the LLL regime. An alternate treatment from Baym and Pethick [25] predicts that  $\mathcal{A}$  saturates at 0.225 as the vortices go from a Thomas-Fermi profile to the profile of a LLL wave function. Our numerical data for  $\mathcal{A}$ , together with experimental points, are plotted in Fig. 4 (a,b). For  $\Gamma_{LLL}^{-1} < 0.1$ , the data agree reasonably well with the Thomas-Fermi result. For larger  $\Gamma_{LLL}^{-1}$ , the data clearly show a smooth transition to the LLL regime, and a saturation of  $\mathcal{A}$  at the LLL limit.

The experimental data in Fig. 4(b) tend to lie above the numerical data. This is likely due to our tendency to overestimate the core size, as discussed previously in Sec. III A. Figure 4(c) demonstrates the dangers of axial expansion in this measurement. For the data presented the condensate undergoes a factor of 2-3 in axial expansion, and we see a corresponding increase in  $\mathcal{A}$ . This clearly illustrates the importance in suppressing axial expansion for these measurements. It is interesting to note that with our rapid axial expansion the fractional core area can overshoot the LLL limit, which in principle should still be valid in the limit of adiabatic expansion.

### C. Core density profile

We can also observe the transition to the LLL regime in the numerical data by examining the shape of the condensate vortex cores. In the Thomas-Fermi regime, the vortex-core density profile is well described by the form  $n(r) = (r/\sqrt{2\xi^2 + r^2})^2$  [20] where  $r$  is measured from the vortex center. Alternatively in the LLL regime, the core is no longer dictated by the interactions but rather by kinetic energy considerations. In this case, within the Wigner-Seitz unit cell, the vortex is thought [25] to have a simple oscillator p-state structure  $n(r) = ((Cr/b) \cdot \exp[-r^2/2l^2])^2$  for  $0 \leq r \leq l$ , where  $C$  is a normalization constant, and  $l$  is the radius of the Wigner-Seitz unit cell and is related to the nearest-neighbor lattice spacing  $b$  by  $l = (\sqrt{3}/2\pi)^{1/2}b$ . Figure 5 is a comparison of the central vortex, in three numerically generated condensates, to both Thomas-Fermi and LLL predicted core shapes. The simulation for Fig. 5(a) was performed for  $3 \times 10^6$  atoms and  $\Omega/\omega_p = 0.15$  and is well inside the Thomas-Fermi regime ( $\Gamma_{LLL} = 117$ ). Here the density profile of the numerical data (solid line) seems to fit quite well to the Thomas-Fermi vortex form (dotted line), but the LLL form is a poor description of the vortex core (dashed line). The simulation for Fig. 5(b) was performed for  $5 \times 10^5$  atoms,  $\Omega/\omega_p = 0.95$  and  $\Gamma_{LLL} = 3.6$ . One can see from Fig. 4 that this is in the transition region. Not surprisingly both vortex forms fit about equally well. In Figs. 5(b) and Fig. 5(c), the vertical line represents the edge of the Wigner-Seitz unit cell at  $r = l$ . The simulation for Fig. 5(c) was performed for  $1 \times 10^5$  atoms,  $\Omega/\omega_p = 0.998$  and  $\Gamma_{LLL} = 0.72$ . One can see that LLL is a much better description of the vortex.

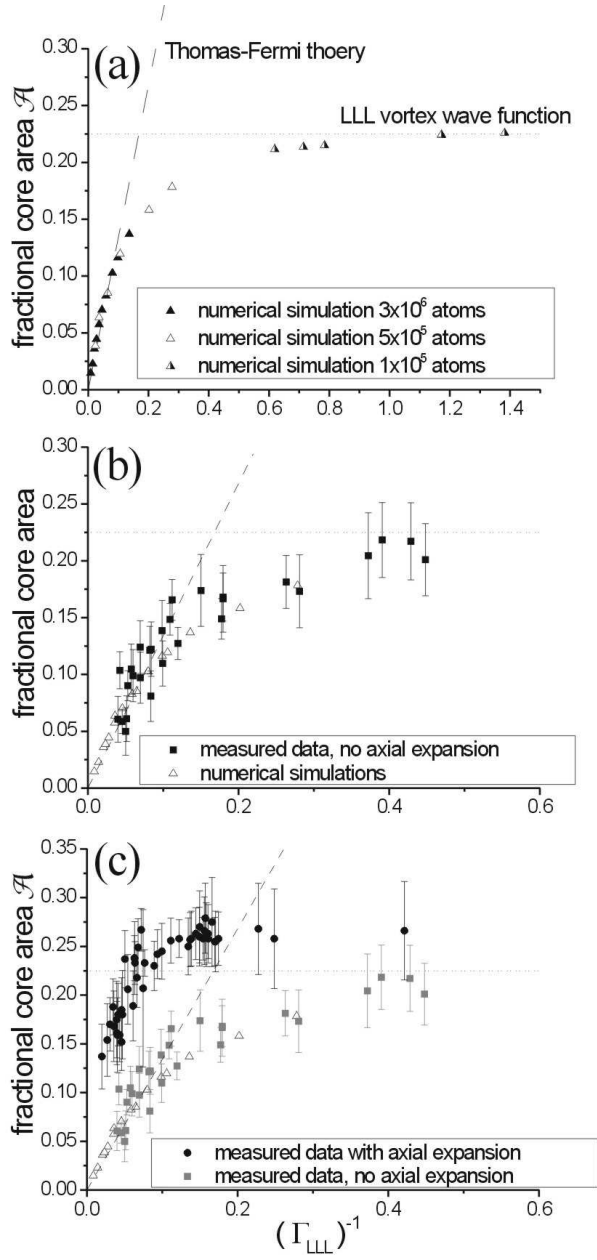


FIG. 4: Fractional condensate area occupied by vortex cores ( $\mathcal{A}$ ) as a function of  $\Gamma_{LLL}^{-1} = 2\hbar\Omega/\mu$ , the inverse lowest Landau level parameter. Plot (a) shows a smooth transition in the numerical data from the Thomas-Fermi limit where  $\mathcal{A}$  is linear in  $\Gamma_{LLL}^{-1}$  to the LLL limit where  $\mathcal{A}$  saturates. Here the Thomas-Fermi theory is represented by the dashed line and the LLL limit by the dotted line. Plot (b) is a comparison of the numerical data to experimental data. Plot (c) demonstrates the effect on the experimental measurement of allowing the condensate to expand axially during the expansion process.

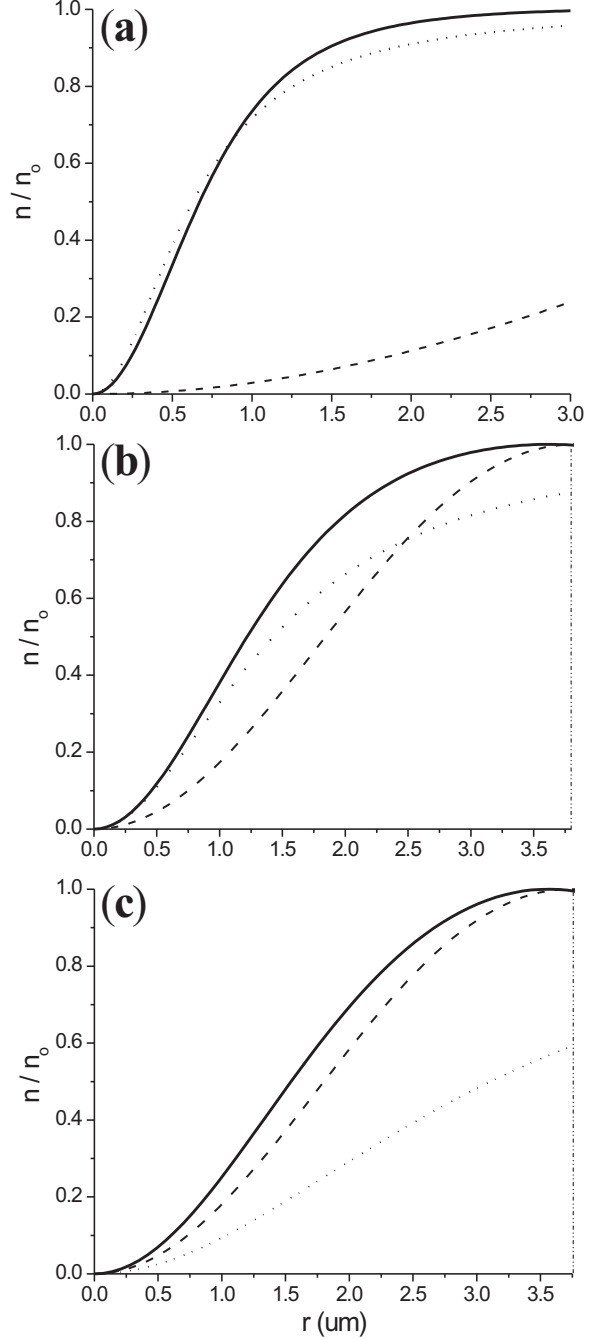


FIG. 5: Numerically generated vortex core density profiles approaching the lowest Landau level regime. Solid lines represent the numerical result for (a)  $\Gamma_{LLL} = 117$ , (b)  $\Gamma_{LLL} = 3.6$ , (c)  $\Gamma_{LLL} = 0.72$ . The dashed line is the expected profile for a LLL wave function [25] given the condensate rotation. The dotted line is the expected vortex form in the Thomas-Fermi limit [20] given the condensate density. The vertical lines in figure (b) and (c) designate the edge of the Wigner-Seitz unit cell. As  $\Gamma_{LLL}$  decreases, one can see a clear transition from the interaction-dominated Thomas-Fermi regime to a LLL function where kinetic energy concerns and the vortex core spacing dictate the shape and size of the vortex.

On a separate but interesting note, even this far into the LLL regime, our numerical solution of the GP equation shows that the radial profile of the overall smoothed condensate fits much better to a parabola than to the Gaussian that was originally predicted [23]. The reason the Gaussian-density-profile prediction fails to pan out can be extrapolated from data presented earlier in this paper. The density-profile prediction for the radial profile in the LLL arose from an elegant argument that was based on an assumption that the vortex nodes were on a perfect triangular lattice. As was originally pointed out to us by A. H. MacDonald [37] and has been the subject of two recent theoretical works [18, 19], a slight radially dependant perturbation in the areal density of vortices is enough to convert a Gaussian density distribution into an inverted parabola. The analytic description of this perturbation in [18] (calculated in the LLL) bears a striking resemblance to the one measured in Sec. II in the Thomas-Fermi regime and also to the analytic form [17] calculated in the Thomas-Fermi regime. The surprising result of this perturbation in the areal density of vortices is that one of the most striking features of the Thomas-Fermi regime, the parabolic Thomas-Fermi density profile, still exists in the LLL regime where the condensate kinetic energy is clearly non-negligible compared to interaction energy.

#### IV. ROTATIONAL SUPPRESSION OF THE QUANTUM DEGENERACY TEMPERATURE

So far in this article, condensate rotation has been considered in terms of its discrete vortex elements and their dynamics. A more global effect of condensate rotation is to suppress the quantum degeneracy temperature,  $T_c$ , for a fixed number of trapped particles,  $N$  [28]. While superficially similar to magnetic-field suppression of  $T_c$  in superconductors, this effect is distinct in that it is not a many-body effect but rather a suppression of atom density due to a rotationally weakened trapping potential.

One can define a static critical temperature,  $T_c^{(0)}$  that applies in the case of no rotation. For a non-interacting gas in a harmonic potential,  $T_c^{(0)} = 0.94\hbar\omega_{ho}N^{1/3}$ , where  $N$  is the number of atoms in the sample and  $\omega_{ho} = (\omega_\rho^2\omega_z)^{1/3}$  is the average trap frequency. Rotational suppression of  $T_c$  may be accounted for by the centrifugal weakening of the radial harmonic confinement,  $\tilde{\omega}_\rho = \omega_\rho\sqrt{1 - \Omega^2/\omega_\rho^2}$ , which leads to a reduction in the thermal gas density  $n_{th}$  relative to the non-rotating case. As a result, for fixed  $N$ , a lower temperature must be reached before the phase space density ( $\sim n_{th}/T^{3/2}$ ) is sufficiently high to bring about the BEC transition. The expression for  $T_c$  as a function of the rigid-body rotation rate  $\Omega$  of the gas sample is

$$T_c = T_c^{(0)}(1 - \Omega^2/\omega_\rho^2)^{1/3}. \quad (5)$$

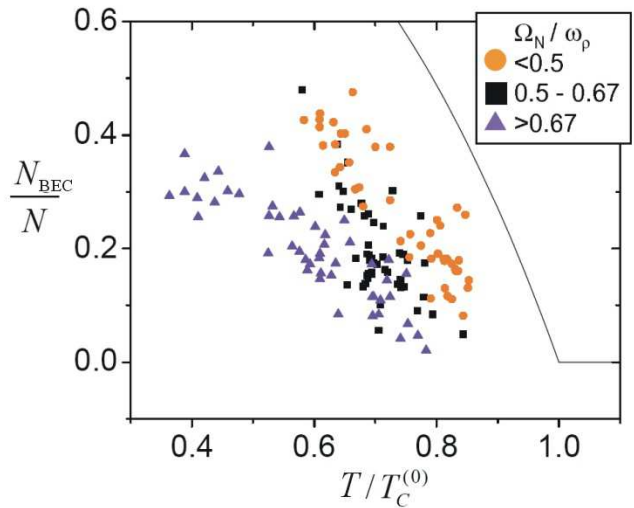


FIG. 6: (Color online) Condensate fraction versus temperature for various sample rotation rates. Condensate number,  $N_{BEC}$ , and total number,  $N$ , are obtained from fits to cloud images. The temperature  $T$  is extracted from the vertical width of the thermal cloud while the centrifugal distortion of the thermal cloud's aspect ratio yields its rotation  $\Omega_N$ . The temperature is scaled by the static critical temperature  $T_c^{(0)}$  for an ideal gas. The data has been grouped according to three different ranges of  $\Omega_N$ . The solid line is the theoretical dependence expected for a static ideal gas.

In Fig. 6, experimental data have been used to plot condensate fraction versus temperature for three different ranges of sample rotation rate. All quantities are obtained from fits to the non-destructive, in-trap images of the trapped gas clouds. As usual, the rotation rate has been assessed from the changing aspect ratio of the thermal cloud according to Eq. 1. It is qualitatively clear from Fig. 6 that a lower temperature is required at higher rotation rates to reach a given condensate fraction. For each data point, the temperature,  $T$ , and condensate fraction,  $N_{BEC}/N$  (where  $N_{BEC}$  is the number in the condensate) can be used together to infer a value for the critical temperature of the sample using the formula  $T_c = [1 - N_{BEC}/N]^{-1/3}T$ . To remove shot-to-shot variation in  $T_c$  due to atom-number fluctuations, the value of the inferred transition temperature can be scaled by the static value  $T_c^{(0)}$  calculated from the measured atom number. The scaled value of  $T_c$  is plotted against rotation rate in Fig. 7 for three ranges of temperature: “hot,” “medium” and “cold,” corresponding to three different ranges of condensate fraction as given by the legend of Fig. 7.

The centrifugal suppression of  $T_c$  is perhaps less interesting than suppression due to many-body interactions. Nevertheless, from a technical stand point, centrifugal effects are an important consideration in the evaporative cooling and spin-up process.

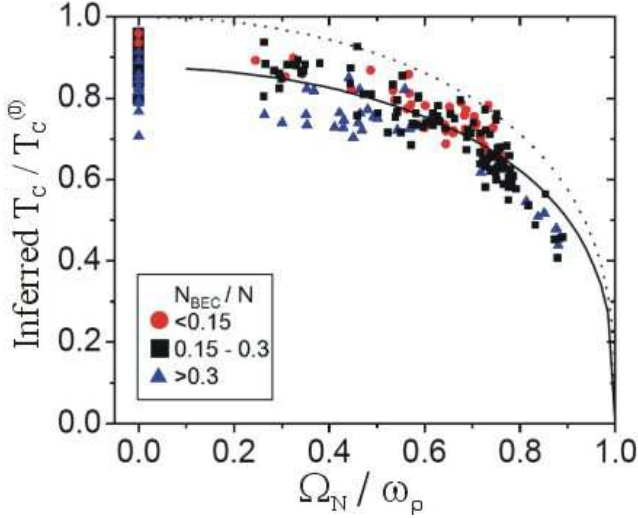


FIG. 7: (Color online) Inferred critical temperature  $T_c$ , scaled by the non-rotating expectation  $T_c^{(0)}$  for an ideal gas, as a function of thermal gas rotation  $\Omega_N$ . For each data point,  $T_c$  is inferred from the measured condensate fraction and temperature of a sample. The total number of atoms is used to obtain  $T_c^{(0)}$ . The data has been grouped according to three different condensate fractions as shown. A set of static points, where the thermal cloud is not stirred before evaporation, are deliberately plotted at zero rotation. Otherwise, the rotation rate  $\Omega_N$  is obtained from the thermal clouds aspect ratio. The rotating data has been cropped at a minimum threshold  $0.2 < \Omega_N/\omega_\rho$  to avoid imaginary rotation values arising from noise in near-static aspect ratios. The dotted line is the theoretical expectation according to Eq. (5) with  $T_c^{(0)}$  as for an ideal gas. The solid line is a fit of the data to Eq. (5) with an arbitrary overall scaling of the vertical axis. The fit result is equivalent to assuming an effective  $T_c^{(0)}$  that is  $87 \pm 1\%$  of the ideal gas value. This 13% shift is consistent with what one would expect from atom-atom interactions [38].

## V. CORE CONTRAST AND CONDENSATE TEMPERATURE

Since the very first observations of dilute-gas BEC, the temperature of the sample has been determined by imaging the “skirt” of thermal atoms that extends beyond the radius of the condensate. In practice, it is difficult to extend this measurement below about  $T/T_c = 0.4$ , except in very special cases (for instance when a Feshbach resonance is used to set the scattering length to zero). For low temperatures, the density of thermal atoms becomes so low that they are difficult to image. Moreover, when the temperature becomes lower than or comparable to the chemical potential of the self-interacting condensate, the spatial extent of the thermal cloud is no longer appreciably larger than the condensate itself.

It was suggested that vortex cores might serve as “thermal-atom concentration pits”, in order to enhance

thermometry at low temperatures. In a simple Hartree-Fock (HF) picture of the interaction between thermal atoms and the condensate, the condensate density represents a repulsive interaction potential to the thermal atoms. Along the nodal line of a vortex core, the condensate density and presumably its repulsive interaction potential vanish. Thus, the thermal atoms would experience the lowest combined interaction and magnetic potential within the cores of vortices. As a result their density would be highest there. Additionally, images of thermal atoms in the vortex core could be taken against a vanishing background condensate density. Moving beyond the HF approximation, one finds a more complicated picture. The Bogoliubov spectrum of very long wave-length thermal phonons extends all the way down to the chemical potential. One should contrast this energy with the energy of a thermal atom confined to a vortex core. Perhaps the atom experiences no interaction energy. However, the kinetic energy cost of bending its wave function to fit inside a core with a radius of the order of healing length must, by definition, be comparable to the chemical potential. In the limit of very elongated vortex cores, there can be very low-energy, core-bending modes [5, 39]. Thermal excitations of these modes would manifest as a temperature-dependent contrast ratio. We expect this effect is unlikely to be important in the relatively flattened geometry of our highly rotating condensates. In any case, without more rigorous analysis, it is not easy to predict how the contrast ratio of our vortices should vary with temperature, but we nonetheless set out to do a preliminary study of the effect.

We vary the final condensate temperature by changing our rf-evaporation end point. This produces a cloud with temperatures between  $5 - 50$  nK or  $T/T_c$  between 1 and less than 0.4. Here  $T_c$  is calculated from the trap frequencies and a measurement of total atom number using the formula  $T_c = 0.94\hbar\tilde{\omega}_{ho}N^{1/3}$ , where  $\tilde{\omega}_{ho}$  has been adjusted for rotation according to the equation  $\tilde{\omega}_{ho} = \omega_{ho}(1 - \Omega^2/\omega_\rho^2)^{1/3}$ . When possible,  $T$  is extracted from a two-component fit to the in-trap image. Because our rotation rate and temperature are linked through the 1D evaporative process, it is unavoidable that  $\Omega$  also varies during the data set.

To measure core contrast, we expand the cloud using the usual expansion procedure. The atom cloud is expanded radially by a factor of 13 to ensure that the cores are large compared to our imaging resolution. However, because we no longer care about the precise core size we do not suppress the axial expansion. Additionally, the axial expansion actually reduces background fluctuations in the measured core contrast. With a factor of two axial expansion, cores become much rounder and clearer as shown in Fig. 1(c). These changes allow us to achieve a higher core contrast and quieter signal than we can without expansion.

The term core brightness (1-contrast ratio) will be our

metric for this experiment. We define core brightness ( $\mathcal{B}$ ) as  $n_{2D}(\text{core})/n_{2D}(\text{cloud})$ , where  $n_{2D}(\text{core})$  is the observed atom density, integrated along the line of sight, at the core center, and  $n_{2D}(\text{cloud})$  is the projected integrated atom density at the same point, based on a smoothed fit to the overall atom cloud. To determine  $n_{2D}(\text{cloud})$ , we fit the condensate image to a Thomas-Fermi profile and the surrounding thermal atoms to a Bose distribution. We find  $n_{2D}(\text{core})$  by fitting each vortex with a Gaussian to determine its center and then averaging five pixels around the center point to determine the integrated density. Brightness is calculated for each vortex and then averaged with other vortices in the cloud. To suppress noise from low signal, vortices further than  $0.4 R_\rho$  from the condensate center are disregarded for this measurement. The  $n_{2D}(\text{core})$  term necessarily contains signal from the surrounding thermal atoms because the vortices do not penetrate the thermal component. Thus, one expects to see a steady decrease in  $\mathcal{B}$  with decreasing temperature, as atoms not necessarily in the vortex core, but still in the integrated line of sight, disappear. One would hope that  $\mathcal{B}$  continues to decrease even for  $T/T_c$  below 0.4 for this analysis to be a viable means of extending condensate thermometry.

We are in the awkward position of comparing our core contrast measurement to a temperature measurement that, as previously described, is expected to fail at low temperatures. To monitor this failure, we calculate a simplistic core brightness ( $\mathcal{B}_{\text{simple}}$ ) found by comparing the fitted in-trap condensate and thermal cloud profiles. Here  $\mathcal{B}_{\text{simple}} \equiv \tilde{n}_{2D}(\text{thermal})/(\tilde{n}_{2D}(\text{condensate}) + \tilde{n}_{2D}(\text{thermal}))$  where  $\tilde{n}_{2D}(\text{condensate})$  and  $\tilde{n}_{2D}(\text{thermal})$  are the smoothed condensate and thermal cloud profiles integrated along the z-axis and averaged over a region of radius less than  $0.4 R_\rho$  from the condensate center. The term  $\mathcal{B}_{\text{simple}}$  can be thought of as the core brightness one would expect based on the undoubtedly false assumption that the condensate and thermal atoms do not interact. It is interesting to compare  $\mathcal{B}$  to  $\mathcal{B}_{\text{simple}}$  since this same dubious assumption is implicit in the standard thermometry technique of fitting the thermal “skirt”.

In Fig. 8,  $\mathcal{B}$  and  $\mathcal{B}_{\text{simple}}$  are plotted versus the final evaporative cut. For our experiment, the thermal cloud can be reliably fit for  $T/T_c > 0.6$  and less reliably fit for  $T/T_c > 0.4$ . In both these regions  $T/T_c$  decreases continuously with lower final evaporative cut. It is assumed that for  $T/T_c$  just below 0.4, this trend continues. For reference, three values of  $T/T_c$  (measured from the thermal “skirt”) are included in the plot. One can see that  $\mathcal{B}$  does steadily decrease with lower temperature for  $T/T_c > 0.4$ . It is interesting to note that  $\mathcal{B}_{\text{simple}}$  closely tracks  $\mathcal{B}$  at the higher temperatures and then diverges from  $\mathcal{B}$  as the cloud gets colder. Presumably, this divergence occurs because thermal atoms are pushed away from the condensate center as interactions between

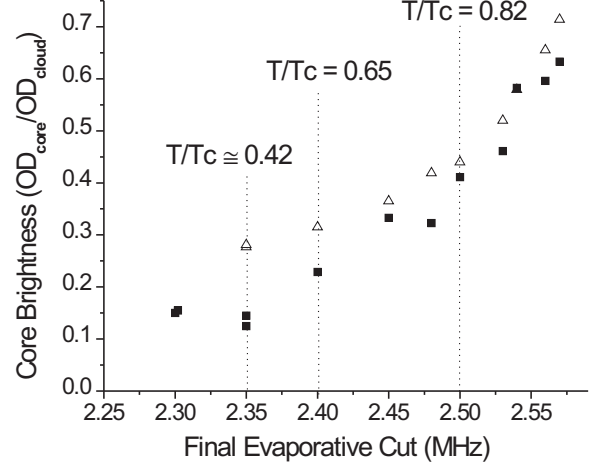


FIG. 8: Measured core brightness as a function of final rf evaporative cut. Within our ability to measure,  $T/T_c$  decreases continuously with the rf frequency. For the black squares brightness ( $\mathcal{B}$ ) is defined as the 2D atom density at the vortex core divided by the 2D atom density of the overall smoothed condensate plus thermal cloud profile at the same point. For the open triangles a simplistic brightness ( $\mathcal{B}_{\text{simple}}$ ) is calculated from the ratio of the 2D atom density of the thermal cloud to the 2D atom density of the overall smoothed condensate and thermal cloud profile. At high temperatures  $\mathcal{B}$  and  $\mathcal{B}_{\text{simple}}$  exhibit a clear dependence on the final rf cut. At lower temperatures it is encouraging that as  $\mathcal{B}_{\text{simple}}$  begins to fail  $\mathcal{B}$  is still continuing a smooth trend downward. Disappointingly at very low temperatures,  $\mathcal{B}$  plateaus at about 0.14.

the condensate and the thermal cloud become important. The fact that  $\mathcal{B}_{\text{simple}}$  diverges upwards is likely due to the tendency of our fitting technique to overestimate the thermal cloud density at high condensate fractions. The failure of  $\mathcal{B}_{\text{simple}}$  at low temperatures also throws into suspicion the quoted  $T/T_c$  since they are determined from the same two-component fit.

In contrast, as  $\mathcal{B}_{\text{simple}}$  begins to fail,  $\mathcal{B}$  continues its previous smooth downward trend. It is also interesting to note that at an rf of 2.35 MHz, we see a  $\mathcal{B}$  of 0.13-0.15, which is not that far off from the work of Virtanen *et al.* [22] who predict that atoms trapped in the core would lead to a  $\mathcal{B}$  of 0.1 at a  $T/T_c$  of 0.39. Unfortunately, our efforts to observe a  $\mathcal{B}$  of less than 0.125 have failed so far, as can be seen from the data points at 2.3 MHz in Fig. 8. This limit impedes our ability to measure temperatures colder than  $0.4 T/T_c$ . Currently, it is unclear what the source of this limit is. Perhaps the same imaging systematics that make our vortex radius unreliable at the 10% level are also preventing us from seeing a core brightness level less than 0.13 or a very slight tilt of the vortices may occur during expansion.

As a caveat to the previous discussion, the same limitations that inhibit condensate thermometry below  $T/T_c$  of 0.4 will also reduce the efficacy of evaporative cooling in the same regime. Additionally, the already inefficient 1D nature of our evaporation would exacerbate such a cooling problem. Perhaps the simplest explanation for the failure of  $\mathcal{B}$  to decrease with very deep rf cuts is that the condensate fraction is no longer increasing. One could imagine the our measured  $\mathcal{B}$  is faithfully following the temperature we achieve.

In summary the conclusions of our preliminary attempt to extend thermometry with core brightness are encouraging but ambiguous. New ideas are needed before we can make further progress.

The work presented in this paper was funded by NSF and NIST. We acknowledge fruitful discussions with Dan Sheehy and Leo Radzihovsky. Numerical simulations were performed with the JILA Keck cluster.

---

[\*] Quantum Physics Division, National Institute of Standards and Technology.

- [1] K. W. Madison, F. Chevy, W. Wohlleben, and J. Dalibard, Phys. Rev. Lett. **84**, 806 (2000).
- [2] J. R. Abo-Shaeer, C. Raman, J. M. Vogels, and W. Ketterle, Science **292**, 476 (2001).
- [3] E. Hodby, G. Hechenblaikner, S. A. Hopkins, O. M. Marago, and C. J. Foot, Phys. Rev. Lett. **88**, 010405 (2002).
- [4] P. C. Haljan, I. Coddington, P. Engels, and E. A. Cornell, Phys. Rev. Lett. **87**, 210403 (2001).
- [5] V. Bretin, P. Rosenbusch, F. Chevy, G. V. Shlyapnikov, and J. Dalibard, Phys. Rev. Lett. **90**, 100403 (2003).
- [6] F. Chevy and S. Stringari, Phys. Rev. A **68**, 053601 (2003).
- [7] R. A. Duine and H. T. C. Stoof, Phys. Rev. Lett. **91**, 150405 (2003).
- [8] J. R. Anglin and M. Crescimanno, cond-mat/0210063.
- [9] I. Coddington, P. Engels, V. Schweikhard, and E. A. Cornell, Phys. Rev. Lett. **91**, 100402 (2003).
- [10] G. Baym, Phys. Rev. Lett. **91**, 110402 (2003).
- [11] S. Choi, L. O. Baksmaty, S. J. Woo, and N. P. Bigelow, Phys. Rev. A **68**, 031605 (2003).
- [12] T. Mizushima, Y. Kawaguchi, K. Machida, T. Ohmi, T. Isoshima, and M. M. Salomaa, Phys. Rev. Lett. **92**, 060407 (2004).
- [13] S. A. Gifford, G. Baym, cond-mat/0405182.
- [14] P. Engels, I. Coddington, P. C. Haljan, and E. A. Cornell, Phys. Rev. Lett. **89**, 100403 (2002).
- [15] P. Engels, I. Coddington, P. C. Haljan, V. Schweikhard, and E. A. Cornell, Phys. Rev. Lett. **90**, 170405 (2003).
- [16] D. L. Feder and C. W. Clark, Phys. Rev. Lett. **87**, 190401 (2001).
- [17] D. E. Sheehy and L. Radzihovsky, cond-mat/0402637.
- [18] G. Watanabe, G. Baym, and C. J. Pethick, cond-mat/0403470.
- [19] N.R. Cooper, S. Komineas, and N. Read, cond-mat/0404112.
- [20] A. Fetter, in *Lectures in Theoretical Physics*, eds. K. Mahanthappa and W.E. Brittin, Vol. XIB, p. 351.
- [21] T. Isoshima and K. Machida, Phys. Rev. A **59**, 2203 (1999).
- [22] S. M. M. Virtanen, T. P. Simula, and M. M. Salomaa, Phys. Rev. Lett. **86**, 2704 (2001).
- [23] T. L. Ho, Phys. Rev. Lett. **87**, 060403 (2001).
- [24] U. R. Fischer and G. Baym, Phys. Rev. Lett. **90**, 140402 (2003).
- [25] G. Baym, C. J. Pethick, cond-mat/0308325.
- [26] J. Sinova, C. B. Hanna, and A. H. MacDonald, Phys. Rev. Lett. **90**, 120401 (2003).
- [27] A.L. Fetter, Phys. Rev. A **64**, 063608 (2001).
- [28] S. Stringari, Phys. Rev. Lett. **82**, 4371 (1999).
- [29] V. Schweikhard, I. Coddington, P. Engels, V. P. Mogenдорff, and E. A. Cornell, Phys. Rev. Lett. **92**, 040404 (2004).
- [30] D. Guery-Odelin and S. Stringari, Phys. Rev. Lett. **83**, 4452 (1999).
- [31] O. M. Marago, S. A. Hopkins, J. Arlt, E. Hodby, G. Hechenblaikner, and C. J. Foot, Phys. Rev. Lett. **84**, 2056 (2000).
- [32] Ellipticity defined as  $(\omega_+^2 - \omega_-^2)/(\omega_+^2 + \omega_-^2)$  where  $\omega_+$  and  $\omega_-$  are the trap frequencies in the along the major and minor trap axes respectively.
- [33] H. J. Lewandowski, D. M. Harber, D. L. Whitaker, E. A. Cornell, J. Low Temp. Phys. **132**, 309 (2003).
- [34] F. Dalfovo, M. Modugno, Phys. Rev. A **61**, 023605 (2000).
- [35] Y. Castin and R. Dum, Phys. Rev. Lett. **77**, 5315 (1996).
- [36] The radial expansion decreases the density, and thus is likely to increase the accuracy of the mean-field treatment. However, once the density has decreased past the point where the chemical potential is small compared to the kinetic energy associated with the finite axial extent the gas enters an effectively 2D regime. In this regime the extent to which microscopic atom-atom correlations subvert the accuracy of the mean-field approximation becomes independent of further reductions in density. This is in contrast to the 3D regime, in which lower density always means better mean-field accuracy, and also in contrast to the 1D regime, in which lower density actually promotes mean-field failure. For the parameters of our experiment (in particular for the case that  $a_{sc} \ll R_z$ ), the effects of correlations in the 2D regime are very small. We thank an anonymous referee for prompting us to look more closely at this limit.
- [37] A. H. MacDonald, private communication.
- [38] F. Gerbier, J. H. Thywissen, S. Richard, M. Hugbart, P. Bouyer, and A. Aspect, Phys. Rev. Lett. **92**, 030405 (2004).
- [39] P. C. Haljan, B. P. Anderson, I. Coddington, and E. A. Cornell, Phys. Rev. Lett. **86**, 2922 (2001).